Autofluorescence Imaging Reflects Metabolic Response to Treatment in Human Head and Neck Squamous Cell Carcinoma

By
Amy Trushar Shah

Thesis
Submitted to the Faculty of the
Graduate School of Vanderbilt University
in partial fulfillment of the requirements
for the degree of

MASTER OF SCIENCE
in
Biomedical Engineering

December, 2013
Nashville, Tennessee

Approved:
Melissa Skala, Ph.D.
H. Charles Manning, Ph.D.

ACKNOWLEDGEMENTS

Funding sources that supported this work include the National Science Foundation (NSF) Graduate Research Fellowship and the Vanderbilt University Start-Up funding for Dr. Melissa Skala. I would like to thank my advisor, Dr. Melissa Skala, for her valuable guidance, encouragement, and expertise in completing this work. I would also like to thank Alex Walsh, Michelle Demory-Beckler, Will Jones, and Paula Pohlmann for their help conducting experiments and insightful conversations. Additionally, I would like to thank the other members of the Optical Imaging Laboratory, particularly Devin McCormack, Kristin Poole, and Jason Tucker-Schwartz, for their positive encouragement during this project. Finally, I would like to thank my parents, Trushar and Dianna, and my brother, Samir, for all their support throughout my personal and academic journeys.

TABLE OF CONTENTS

LIST OF TABLES

Table Page

LIST OF FIGURES

CHAPTER 1

INTRODUCTION

Anatomy and Physiology of the Head and Neck

Epithelial Tissue Structure and Function

Epithelial cells cover the outside of the body and line the organs and cavities, including the oral cavity, throat, and nasal cavity [1]. They are located close to each other, and the membranes of adjacent epithelial cells join together to create tight junctions [1]. Epithelial cells serve to protect the body from foreign intruders and mechanical damage from outside the body as well as to form glands, which serve the function to secrete or absorb. Cell shape and the number of cell layers are criteria used for describing epithelial cells. Simple epithelium describes a single layer of cells, whereas stratified epithelium describes multiple layers of cells. Epithelial cells can be cuboidal (cube-shaped), columnar (shaped like a rectangular prism), or squamous (flat and long) [2]. Figure 1 illustrates the difference between these cell types. Squamous cells create linings for organs and allow for diffusion across these barriers [3]. Additionally, epithelial cells exhibit polarity, in which an apical membrane faces the lumen, whereas the basolateral membrane faces the basement membrane [4].

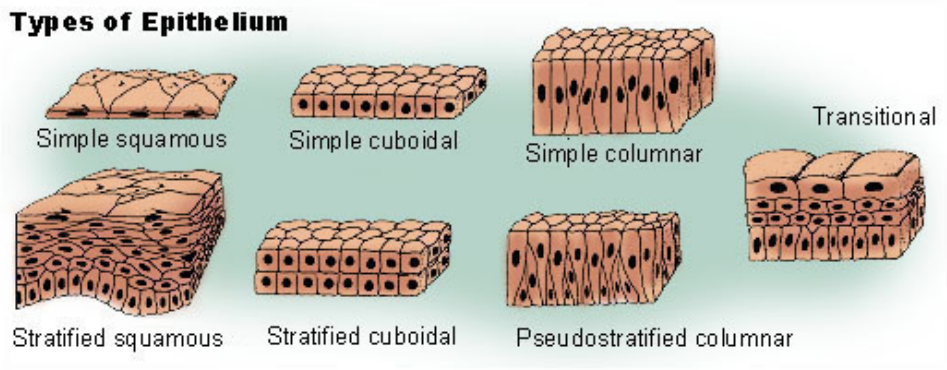

Figure 1: Epithelial cell characterization. Epithelial cells are characterized by their shape and number of layers [2].

More than 85% of cancers originate in the epithelium [5]. One side of the epithelia is exposed to the exterior environment, and the other side of the epithelia is adjacent to the basement membrane (Figure 2). Metastasis can occur after cancer cells break through basement membrane. The epithelial layer is avascular.

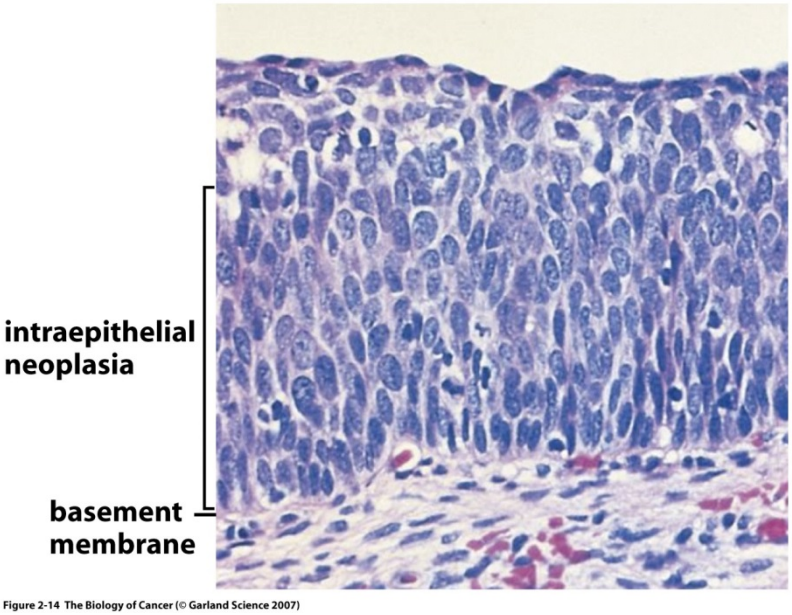

Figure 2: Anatomy of epithelial cells. Epithelial cells are exposed on one side and adjacent to the basement membrane on the other side [6].

Head and Neck Anatomy and Physiology

The head and neck region includes the nasal cavity, oral cavity, pharynx, and larynx. These organs work together to perform critical functions, including chewing and swallowing food, speaking, and breathing.

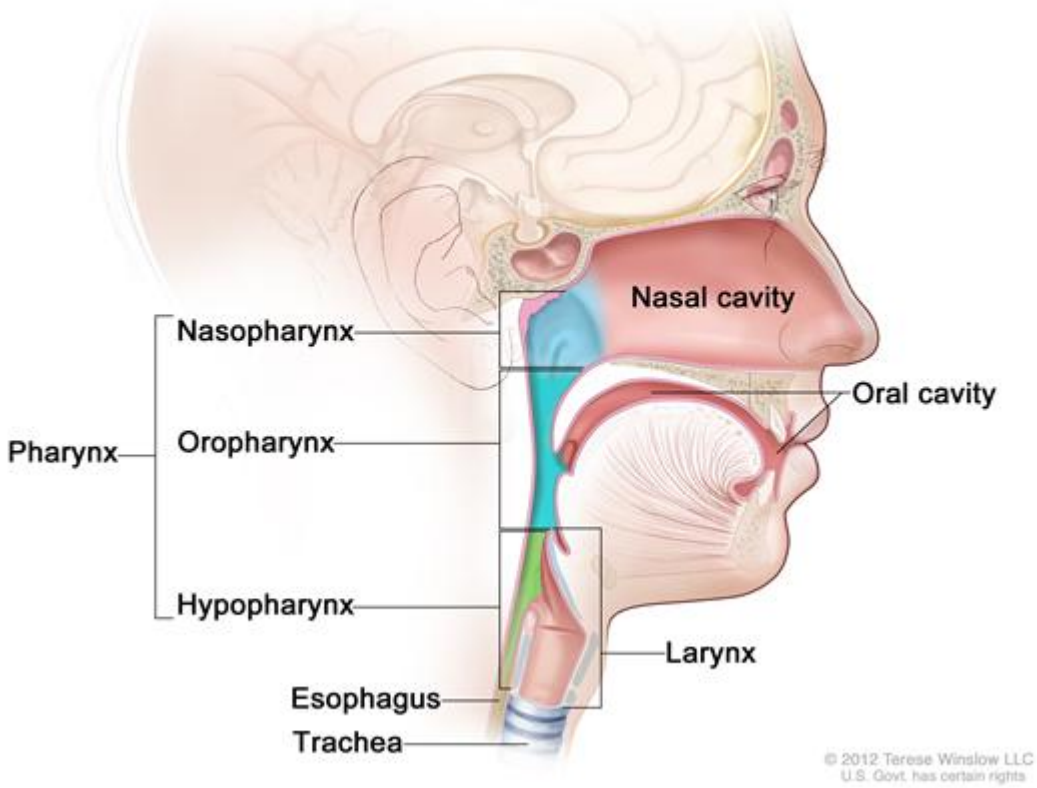

Figure 3: Anatomy of the head and neck region. Head and neck squamous cell carcinoma originates in squamous cells of the oral cavity, nasal cavity, pharynx, and larynx [7].

The oral cavity includes the lips, teeth, jaw, tongue, roof of the mouth, floor of the mouth, and salivary glands. The lips form the opening of the mouth and they are important in speech and

containing food in the mouth. The tongue helps guide food and contains taste buds. The main function of the oral cavity is to chew and break down food mechanically using teeth and chemically using saliva produced by salivary glands.

The pharynx is a five-inch long tube located between the nose and the esophagus, and it consists of the nasopharynx, oropharynx, and hypopharynx. This cavity in the throat connects the nasal and oral cavities with the rest of the respiratory and digestive system, including the stomach, small intestine, and large intestine. Swallowing occurs in the pharynx, moving food from the mouth into the esophagus.

The larynx is situated below the pharynx. It is also called the voice box because it contains vocal chords that create sound and control pitch and volume. During swallowing, the larynx is elevated and the vocal chords move towards each other to move food through the esophagus and prevent it from going into the trachea, which leads to the lungs. The epiglottis, a layer of cartilage, moves over the laryngeal opening to prevent food from going into the respiratory pathways. The esophagus connects the pharynx to the stomach, where food is stored and broken down.

Head and Neck Squamous Cell Carcinoma

Risk Factors and Diagnosis

Head and neck squamous cell carcinoma (HNSCC) originates in squamous cells of the oral cavity, nasal cavity, pharynx, and larynx. The hallmarks of cancer include evading apoptosis, self-sufficiency in growth signals, insensitivity to anti-growth signals, tissue invasion

and metastasis, and limitless replicative potential [6]. More than 90% of head and neck cancers are squamous cell carcinoma [8].

Incidence and mortality of HNSCC is correlated with long-term use of tobacco and alcohol. About 75% of HNSCC incidence occurs in men compared with 25% in women [9]. The stereotypical HNSCC patient is above 50 years old, but the younger population of HNSCC patients is increasing. In particular, this increase has been attributed to the prevalence of human papilloma virus (HPV), which affects about 25% of HNSCC cases [10][11]. Additionally, poor diet, particularly lacking vitamin A and iron, and poor oral hygiene can increase risk for developing HNSCC [12].

Early symptoms of HNSCC are usually vague. Symptoms of cancer in the oral cavity include persistent abnormal masses and sores [13]. Symptoms of cancer in the oropharynx, hypopharynx, and larynx include difficulty swallowing, sore throat, and hoarseness or other changes in voice quality. Symptoms of cancer in the nasal cavity include difficulty breathing through the nose and inflammation of the sinuses [14]. Screening is conducted using physical examination to inspect ulcers within the mouth and throat, palpation of the neck, and endoscopy. Additionally, magnetic resonance imaging (MRI), x-ray, and computed tomography (CT) can be used to detect HNSCC [15]. HNSCC is diagnosed by pathologic examination of surgical biopsy. Unfortunately, most cases are diagnosed at advanced stages, so effective treatment options are crucial to prevent unnecessary mortality and morbidity.

Treatment Techniques and Monitoring of Response

Treatment techniques for HNSCC depend on the stage, location, and resectability of the primary tumor. Early stages are usually treated with surgery to remove tumor-containing tissue and radiation, while advanced stages are treated with surgery and radiation in combination with chemotherapy, including cisplatin and fluorouracil (FU). Targeted therapies have also been investigated. HNSCC exhibits upregulation of epidermal growth factor receptor (EGFR) in more than 90% of cases [16]. EGFR activation leads to growth and proliferation of epithelial cells (Figure 4). Cetuximab is a monoclonal antibody that binds to EGFR, prevents activation, and leads to receptor degradation, and it has been used to inhibit EGFR-expressing tumors. Cetuximab is approved in combination with radiation therapy in patients with locally advanced HNSCC. However, since only a portion of patients respond to EGFR inhibitors, downstream targets have the potential to improve patient outcomes. Commonly mutated targets include phosphoinsitide 3-kinase (PI3K), signal transducer and activator of transcription 3 (STAT3), mammalian target of rapamycin (mTOR), Akt, vascular endothelial growth factor receptor (VEGFR), NF-κB, and human epidermal growth factor receptors 2 (HER2) and 3 (HER3) [17] [18].

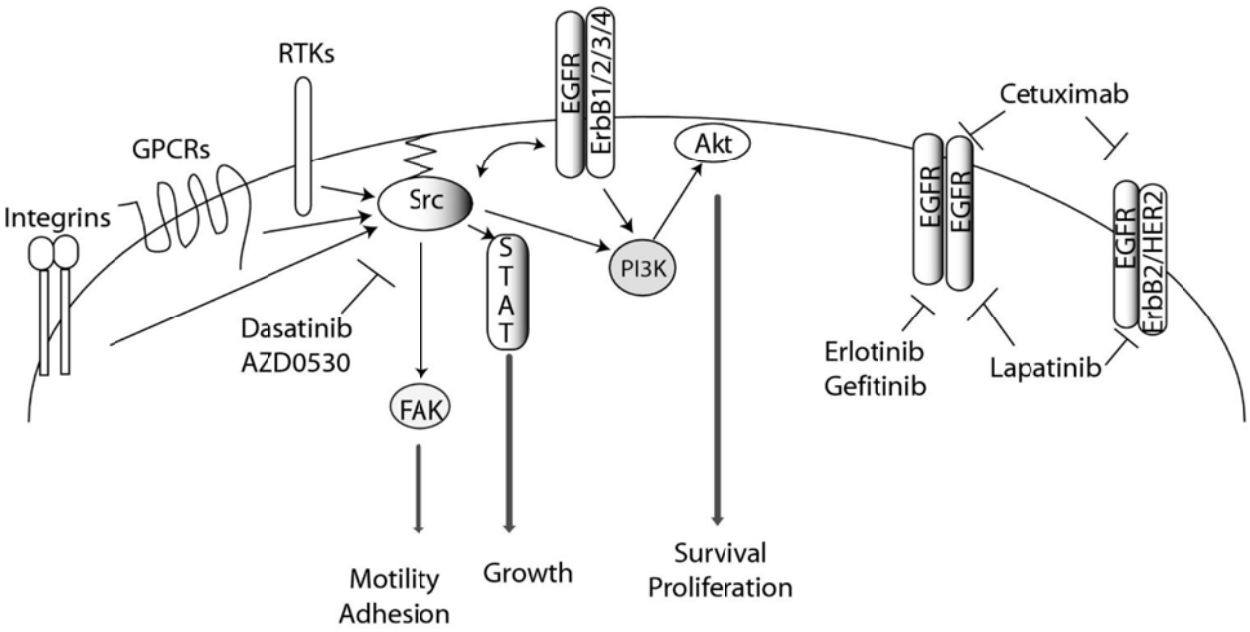

Figure 4: EGFR signaling pathway. EGFR activates pathways promoting cell survival and proliferation [19].

Current treatment options introduce toxicities and complications that impair the patient's quality of life. Surgeries often lead to serious morbidities, including difficulty or inability to speak and swallow, swelling, and changes in appearance. Therefore, organ preservation and function preservation are important considerations in HNSCC treatment. Additionally, radiotherapy and chemotherapy cause side effects, such as nausea, diarrhea, rash, dry mouth or thickened saliva, or changes in taste [13]. HNSCC can be aggressive depending on the location and proximity to lymph nodes, increasing the capability to metastasize [20]. The 5-year survival rate for HNSCC patients is between 40-50% [21]. Despite advancements and improvements in surgical techniques, chemotherapy, and radiation delivery, long-term survival has not improved [22]. The current standard to measure cancer treatment response includes whole-body imaging methods, like CT, x-ray, MRI, and positron emission tomography (PET).

Optical Techniques for Head and Neck Squamous Cell Carcinoma

Detection of Head and Neck Squamous Cell Carcinoma

HNSSC is an ideal target for optical imaging because of easy access to the site using fiber optic probes [23][24]. Additionally, fiber optics can be incorporated into endoscopes that are currently in use.

Optical techniques have been investigated to detect HNSCC. High-resolution microendoscopic imaging has been used to distinguish cancerous versus benign sites for assessing tumor margins in surgery for HNSCC [23]. Additionally, fluorescence spectroscopy has been shown to identify oral neoplasias with sensitivities and specificities greater than 88% [25]. Reflectance spectroscopy using polarized light has also been shown to non-invasively extract morphologic information to detect neoplasia in epithelial tissue phantoms and oral tissue *in vivo* [26]. Muller, ***et al.*** combined intrinsic fluorescence spectroscopy, diffuse reflectance spectroscopy, and light scattering spectroscopy and achieved a sensitivity and specificity of 96% and 96% in distinguishing dysplasia from normal tissue in HNSCC patients [27]. Contrast agents, particularly acetic acid, and blue-white light have been used to identify premalignancy in the oral cavity, but clinical studies will be required to determine the sensitivity and specificity of these techniques [28].

Attempts have been made to monitor treatment response in HNSCC using fluorescently-labeled antibodies. In one study, mice with HNSCC xenografts treated with fluorescently-labeled cetuximab decreased in tumor size, but tumor fluorescence did not correlate with response to treatment [29]. Gleysteen *et al.* used a similar approach of growing xenografts and treating the mice with fluorescently labeled cetuximab, cisplatin, and radiation. They found no change

among fluorescence intensity before treatment, after six weeks of treatment, or at ten weeks of treatment, although tumor regression was observed based on histological analysis. This indicates that fluorescence intensity of labeled cetuximab does not reflect tumor response [30]. However, endogenous fluorescence has not been studied to measure treatment response in HNSCC.

Two-Photon Fluorescence Microscopy and Fluorescence Lifetime Imaging

Light can be described as packets of energy in photons. Fluorescence occurs when a molecule absorbs a photon of a particular energy and emits a photon of a different energy [31]. This absorption excites the molecule from the ground state, S, to the excited state, S*, and upon relaxation the emitted light has an energy less than the absorbed energy (Figure 5). Energy and wavelength are inversely related according to $E = hc/\lambda$, where E represents energy, h represents Planck's constant, λ represents wavelength, and c represents the speed of light. Therefore, a lower energy corresponds to a longer wavelength. Endogenous fluorophores, including NADH, FAD, tryptophan, collagen, and elastin, occur naturally in the body, and probing these can eliminate the need for dyes or contrast agents [32].

Two-photon excitation occurs by simultaneous absorption of two photons with half the energy required for single-photon excitation (Figure 5) [33]. Photons with half the energy correspond to twice the wavelength. Most endogenous fluorophores are excited in the ultraviolet (UV) to visible range (~300-500nm), so therefore two-photon excitation uses near-infrared (NIR) light (~700-900nm) for excitation [32]. UV or visible light is constrained to a penetration depth of about 100μm below tissue surface, whereas decreased scattering and absorption for NIR light allows for deeper penetration [34]. Additionally, since the absorption of two photons is required

for excitation, sufficient photon flux is only present at the focal point, whereas single-photon excitation can produce fluorescence outside the focal point due to scattering (Figure 6). This allows for precise depth-sectioning and elimination of out-of-focus signal.

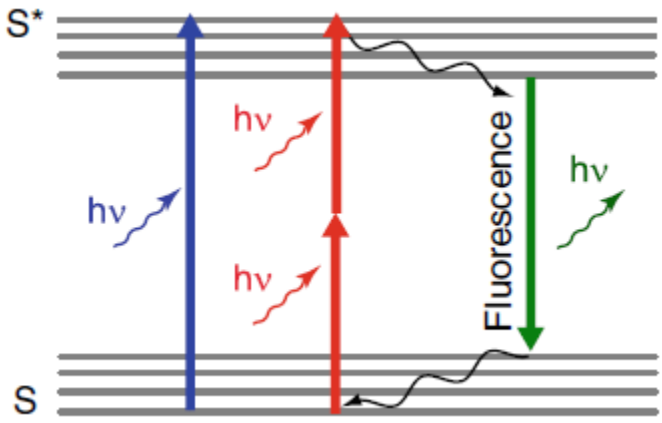

Figure 5. Absorption and fluorescence emission energy diagram. Single-photon (blue) and two-photon (red) excitation causes fluorescence emission (green) [35].

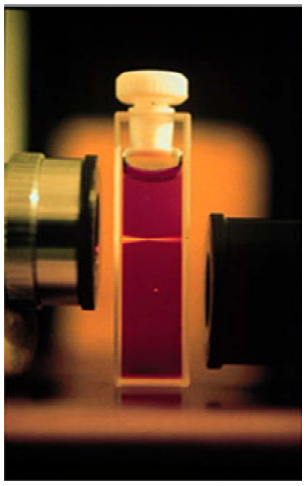

Figure 6. Comparison between single-photon and two-photon excitation. Single-photon fluorescence causes excitation at the focal point and outside the focal point (top), whereas two-photon fluorescence causes excitation only at the focal point (bottom) [36].

Fluorescence lifetime imaging probes the amount of time that a fluorophore is in the excited state before relaxing to the ground state [31][37]. The lifetime is sensitive to the microenvironment, including protein-binding, pH, and oxygen. In particular, the lifetime discriminates between free and protein-bound conformations of molecules. To calculate the lifetime, a histogram of the lifetime events is plotted and fit to an exponential curve. The number of components in the exponential curve depends on the number of molecular species or binding configurations present. For example, NADH and FAD exist in free and protein-bound conformations, so these lifetime histograms are fit to a two-component exponential function: $F(t) = \alpha_1 e^{-t/\tau 1} + \alpha_2 e^{-t/\tau 2}$, where F represents the fluorescence as a function of time, α represents the contribution from each component and τ represents the lifetime of each component (figure 7). The lifetime occurs on the order of picoseconds to nanoseconds. Applying two-photon fluorescence and fluorescence lifetime imaging of the metabolic cofactors NADH and FAD can provide insight into cellular metabolism and microenvironment *in vitro* and *in vivo* [38].

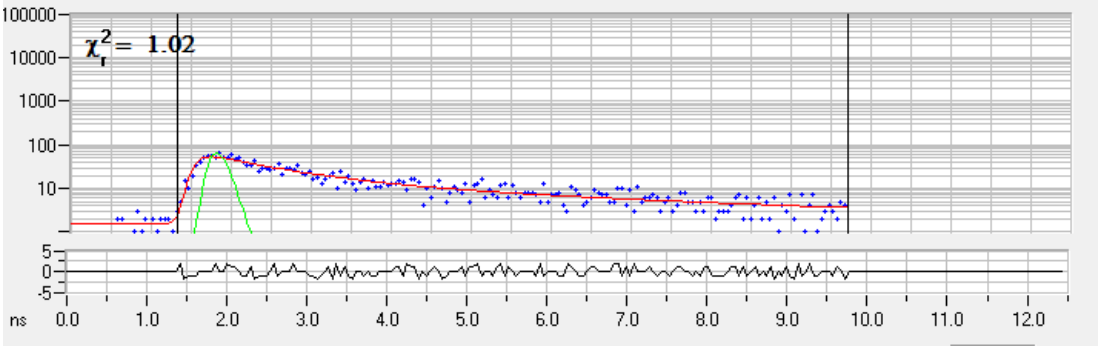

Figure 7. Fluorescence lifetime decay curve. The fluorescence lifetime is calculated by fitting the lifetime events (blue) to an exponential function (red).

CHAPTER 2

OPTICAL METABOLIC IMAGING OF TREATMENT RESPONSE IN HUMAN HEAD AND NECK SQUAMOUS CELL CARCINOMA

Introduction

Head and neck squamous cell carcinoma (HNSCC) is the sixth leading cancer by incidence in the world [21]. Each year, 500,000 new cases are diagnosed with a five-year survival rate between 40-50% [21]. Current standards of care for HNSCC patients include surgery, radiation therapy, and chemotherapy. However, surgeries often cause serious morbidities by impairing the ability to speak, chew, and swallow. Additionally, radiation therapy and chemotherapy introduce toxicities causing nausea, diarrhea, rash, dry mouth or thickened saliva, and changes in taste [13]. These negative side effects from HNSCC treatment justify the need for improved treatments and the development of biomarkers of early treatment efficacy.

Current measures of treatment response in HNSCC include x-ray computed tomography (CT), magnetic resonance imaging (MRI), and positron emission tomography (PET). However, these methods are only effective weeks to months after treatment begins and require contrast agents and/or expensive equipment. Alternative treatment options for non-responders include re-irradiation, chemotherapy, or surgery [39]. Early predictors of drug efficacy would reduce toxicities, costs, and time associated with ineffective therapy. Therefore, there is a need for a cost-effective, noninvasive tool to determine treatment response at an early timepoint.

Therapeutic interventions for HNSCC include traditional chemotherapy and targeted inhibitors. Cisplatin is a common chemotherapy used in HNSCC [40]. In the past decade,

targeted inhibitors have been developed to treat HNSCC. More than 90% of HNSCC cases exhibit upregulation of epidermal growth factor receptor (EGFR). The EGFR signaling pathway drives cell proliferation, growth, and survival. EGFR is the only proven molecular target for HNSCC therapy [39]. Cetuximab is a monoclonal antibody that inhibits EGFR activation, but clinical outcomes with cetuximab treatment have been poor and are not correlated with EGFR protein expression levels [41]. Therefore, downstream effectors, including phosphatidylinositol 3-kinase (PI3K) and mammalian target of rapamycin (mTOR), have been investigated as potential therapeutic targets. PI3K, a master regulator of metabolism, is mutated in about 37% of HNSCC [42]. BGT226 is a PI3K/mTOR inhibitor currently under clinical investigation for solid tumors [43]. However, there is a need for improved technologies to guide the selection of drugs for individual patients, so that alternative treatments such as BGT226 can be used at an early timepoint.

The EGFR and PI3K/mTOR signaling pathways regulate cellular metabolism, including glycolysis and oxidative phosphorylation. Cancer often exhibits altered metabolism, particularly increased aerobic glycolysis (Warburg effect) [44]. During glycolysis, NAD^+ is reduced to nicotinamide adenine dinucleotide (NADH). During oxidative phosphorylation, NADH is oxidized to NAD^+ and $FADH_2$ is oxidized to flavin adenine dinucleotide (FAD). NADH and FAD exhibit autofluorescence, whereas NAD^+ and $FADH_2$ do not. The optical redox ratio, defined as the fluorescence intensity of NADH divided by the fluorescence intensity of FAD, reflects relative amounts of glycolysis compared with oxidative phosphorylation and is an established method for probing cellular metabolism [38][45][46]. The fluorescence lifetime is the time a fluorophore stays in the excited state before relaxing to the ground state and reflects fluorophore microenvironment, including protein-binding and preferred metabolic pathways

[31]. The optical redox ratio and fluorescence lifetimes of NADH and FAD exploit intrinsic contrast to measure optical endpoints of cellular metabolism. Furthermore, metabolic endpoints show particular promise because shifts in cellular metabolism often occur sooner than changes in tumor size or glucose uptake.

Tissue autofluorescence has been previously used to detect HNSCC. The autofluorescence intensity of NADH and FAD has been used to distinguish normal from dysplasia in oral tissue [47], and the NADH and FAD fluorescence lifetimes have been shown to identify precancer compared with normal in the DMBA-treated hamster cheek pouch model [48][49][50][51]. Multiphoton microscopy of endogenous fluorescence has been used to quantify cellular and tissue morphology in the DMBA-treated hamster cheek pouch model [52][53]. However, no previous literature has characterized endogenous fluorescence in response to treatment in HNSCC. Fluorescent dyes have been used to monitor anti-EGFR antibody uptake in HNSCC, but results did not reflect response *in vivo* [29][30]. Optical metabolic imaging is sensitive to early metabolic shifts after cancer treatment and has potential to noninvasively detect treatment response sooner than current methods.

The serious morbidities and toxicities from HNSCC treatment justify the need for early predictors of treatment efficacy. This study tests the hypothesis that autofluorescence from metabolic cofactors NADH and FAD can resolve response to targeted therapies and chemotherapy in HNSCC. Optical metabolic imaging was performed on two HNSCC cell lines, SCC25 and SCC61, treated for 24 hours with targeted drugs (cetuximab or BGT226) or chemotherapy (cisplatin). HNSCC is an ideal site for optical imaging because of easy access to the site with fiber optic probes. These results indicate that optical metabolic imaging has

potential to expedite drug screenings, develop optimal treatments, and improve patient outcomes for HNSCC.

Materials and Methods

Cell Culture and Reagents

The TERT-immortalized human oral keratinocyte line OKF6/TERT-1 (OKF6), the squamous cell carcinoma line SCC25, and the squamous cell carcinoma line SCC61 were acquired from J. Rheinwald and the Cell Culture Core of the Harvard Skin Disease Research Center, Boston, MA [54]. OKF6 cells were cultured in keratinocyte serum-free medium (GIBCO K-sfm; Invitrogen) supplemented with 25μg/ml bovine pituitary extract, 1% penicillin/streptomycin, 0.2ng/ml epidermal growth factor, and 0.3mM $CaCl_2$. SCC25 and SCC61 cells were cultured in DMEM/F12 media (Invitrogen) supplemented with 10% fetal bovine serum and 0.4μg/ml hydrocortisone (Sigma).

For fluorescence imaging, 10^5 cells were plated on 35 mm glass-bottomed dishes (MatTek Corp.). The media was replaced 24 hours after plating with control media or treatment media containing 13nM (1.90 μg/mL) cetuximab (Vanderbilt Pharmacy), 300nM NVP-BGT226 (Selleckchem), or 176μM cisplatin (Selleckchem). The drug doses were chosen to be 11 times the IC50 for each drug [55] [56] [57]. The cells were imaged 24 hours after treatment.

Imaging Instrumentation

Fluorescence lifetime images were collected using a custom-built multi-photon fluorescence microscope (Prairie Technologies). Images were acquired through an inverted

microscope (TiE, Nikon) with a 40x oil immersion objective (1.3 NA). Fluorescence was excited using a titanium:sapphire laser (Chameleon, Coherent Inc.) and collected using a GaAsP photomultiplier tube (H7422P-40, Hamamatsu). NADH and FAD images were acquired sequentially for the same field of view. NADH fluorescence was isolated using an excitation wavelength of 750nm and an emission bandpass filter of 400-480nm. FAD fluorescence was isolated using an excitation wavelength of 890nm and an emission bandpass filter of 500-600nm. The average power incident on the sample was approximately 10mW. The acquired images consisted of 256 x 256 pixels (170μm x 170μm) with a 4.8μs pixel dwell time. Time-correlated single photon counting (TCSPC) electronics (SPC-150, Becker and Hickl) were used to collect fluorescence lifetime images over 60 seconds. The absence of photobleaching was confirmed by monitoring photon count rates throughout image acquisition.

The instrument response function (IRF) was measured from second harmonic generation of urea crystals excited at 900nm, and the full width at half maximum (FWHM) was calculated to be 244 ps. A Fluoresbrite YG microsphere (Polysciences Inc.) was imaged as a daily standard. The lifetime decay curves were fit to a single exponential decay and the fluorescence lifetime was measured to be 2.13 ± 0.28ns (n=7), which is consistent with published values [49][58].

Cyanide Perturbation

The OKF6 cells were plated at a density of 10^5 cells per 35 mm glass-bottomed dish (MatTek Corp.). After 48 hours, fluorescence lifetime images of NADH and FAD were acquired. Then, the media was replaced with cyanide-supplemented media (4mM NaCN, Sigma). After five minutes of cyanide treatment, fluorescence lifetime images of NADH and FAD were acquired.

Image Analysis

Fluorescence lifetime images were analyzed using SPCImage software (Becker and Hickl). Binning included the selected pixel and the eight surrounding pixels. The fluorescence lifetimes were calculated by de-convolving the measured fluorescence decay curve with the IRF and fitting to a two-component exponential curve, $F(t) = \alpha_1 e^{-t/\tau 1} + \alpha_2 e^{-t/\tau 2} + c$. F(t) represents the fluorescence intensity as a function of time after the excitation pulse, τ_1 and τ_2 represent the short and long fluorescence lifetimes, respectively, α_1 and α_2 represent the contribution from each lifetime component ($\alpha_1+\alpha_2=1$), and c represents background light. A two-component decay curve was chosen to represent free and protein-bound conformations of NADH and FAD [49]. The weighted mean lifetime, τ_m, was calculated, $\tau_m = \alpha_1\tau_1+\alpha_2\tau_2$. The photon counts per pixel were summed over the 60 second collection time to calculate a fluorescence intensity image. A threshold was applied to exclude fluorescence from background and cell nuclei. The fluorescence intensities and lifetime values were imported into MATLAB (Mathworks) for further quantification. Redox ratio images were calculated by dividing the fluorescence intensity image of NADH by the fluorescence intensity image of FAD for the same field of view, and the average per image was computed. The redox ratio was normalized to control cells for comparing treatment groups within cell lines. The redox ratio was normalized to the nonmalignant OKF6 cells when comparing between cell lines. Average fluorescence lifetime values were calculated per image.

Western Blotting Analysis

Cells were plated at $3*10^6$ cells per 10cm dish. After 24 hours, the media was removed, the cells were washed three times with phosphate buffered saline (PBS), and serum-free media was added. After another 24 hours, the media was replaced with treatment media for one hour. For the groups treated with epidermal growth factor (EGF) or transforming growth factor alpha (TGF-α), 10ng/mL EGF or TGF-α was added for 5 minutes. The cells were lysed with lysis buffer (1% Triton X-100, 10% Glycerol, 50 mM HEPES pH 7.2, and 100 mM NaCl) supplemented with sodium orthovanadate and protease inhibitor cocktail. Proteins were separated using a 10% SDS-PAGE separation gel at 100V. The gel was transferred at 27V overnight to a PVDF membrane. The membrane was blocked using 5% bovine serum albumin (BSA) for one hour and then incubated in the following primary antibodies overnight: EGFR (Millipore, 1:1000), pY1173 EGFR (Cell Signaling, 1:250), AKT (Cell Signaling, 1:250), pS473 AKT (Cell Signaling, 1:250), or GAPDH (Sigma, 1:1000). Membranes were washed four times and secondary antibodies added for one hour, and electrogenerated chemiluminescence (ECL) was used to measure luminescence.

Proliferation Assay

Cells were plated in a 96 well plate at $3.3*10^3$ cells per well. Four wells per treatment group were plated. After 24 hours, the media was replaced with treatment media supplemented with 10μM BrdU. The cells incubated for 24 hours and then were fixed with 4% paraformaldehyde for 15 minutes. The cells were washed twice with PBS and permeabilized with 0.3% Triton X in PBS for 15 minutes. The DNA was denatured using hydrochloric acid, and the cells were blocked using 10% goat serum and 0.3% Triton X for one hour. Primary

antibody (rat anti-BrdU, Abcam, 1:100) was incubated overnight. The cells were washed three times with PBS and incubated in secondary antibody (DyLight594-conjugated goat anti-rat, Jackson Immunoresearch, 1:200) for two hours. The cells were washed three times with PBS and counterstained with Hoechst 33528 (1:1000) for 10 minutes. Fluorescence images were acquired for three fields of view per well (n=12), and the number of cells per image was counted (ImageJ).

Glucose and Lactate Assays

Cells were plated at a density of 10^5 cells per 35 mm dish, and 24 hours later the media was replaced with treatment media. After 24 hours of treatment, glucose and lactate concentrations were measured according to the protocols of commercially available kits (Invitrogen; Eton Biosceience).

Statistical Analyses

Bar graphs are represented as mean ± standard error. Statistical significance was determined using two-way Wilcoxon rank sum tests in MATLAB (Mathworks). A p-value less than 0.05 indicated statistical significance.

Results

Redox ratio validation was performed by perturbing nonmalignant OKF6 cells with 4mM cyanide, which prevents oxidation of NADH to NAD^+ in the electron transport chain [59]. This accumulation of NADH causes an increase in the optical redox ratio (Figure 8a) and verifies isolation of NADH and FAD fluorescence. The contribution from free NADH (α_1) increases with

cyanide treatment (Figure 8b), causing a decreased NADH mean lifetime (data not shown). The contribution from protein-bound FAD (α_1) decreases with cyanide treatment (Figure 8c), causing an increased FAD mean lifetime (data not shown).

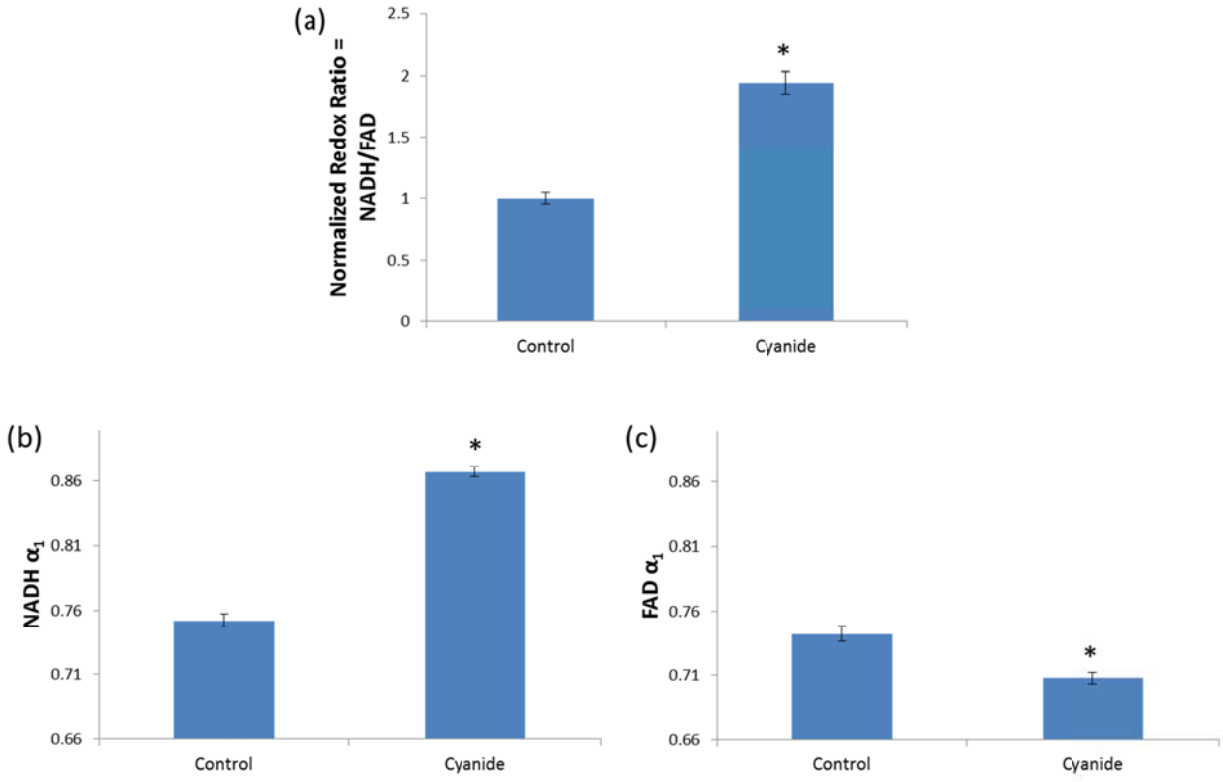

Figure 8. Cyanide treatment alters redox ratio, NADH α_1, and FAD α_1 in nonmalignant oral cells (OKF6). (a) Cyanide treatment (4mM) disrupts the electron transport chain, causing an increase in the optical redox ratio. (b) Cyanide treatment increases the contribution of free NADH (α_1) and (c) decreases the contribution of protein-bound FAD (α_1). * $p<0.05$, rank sum test; mean ± SEM.

The optical metabolic endpoints differentiate the malignant cell lines, SCC25 and SCC61, from the nonmalignant cell line, OKF6 (Figure 9). The malignant cell lines showed an increased redox ratio compared with the OKF6 cells ($p<0.05$). The malignant cell lines showed

increased NADH α_1 compared with the OKF6 cells ($p<0.05$) and increased FAD α_1 compared with the OKF6 cells ($p<0.05$).

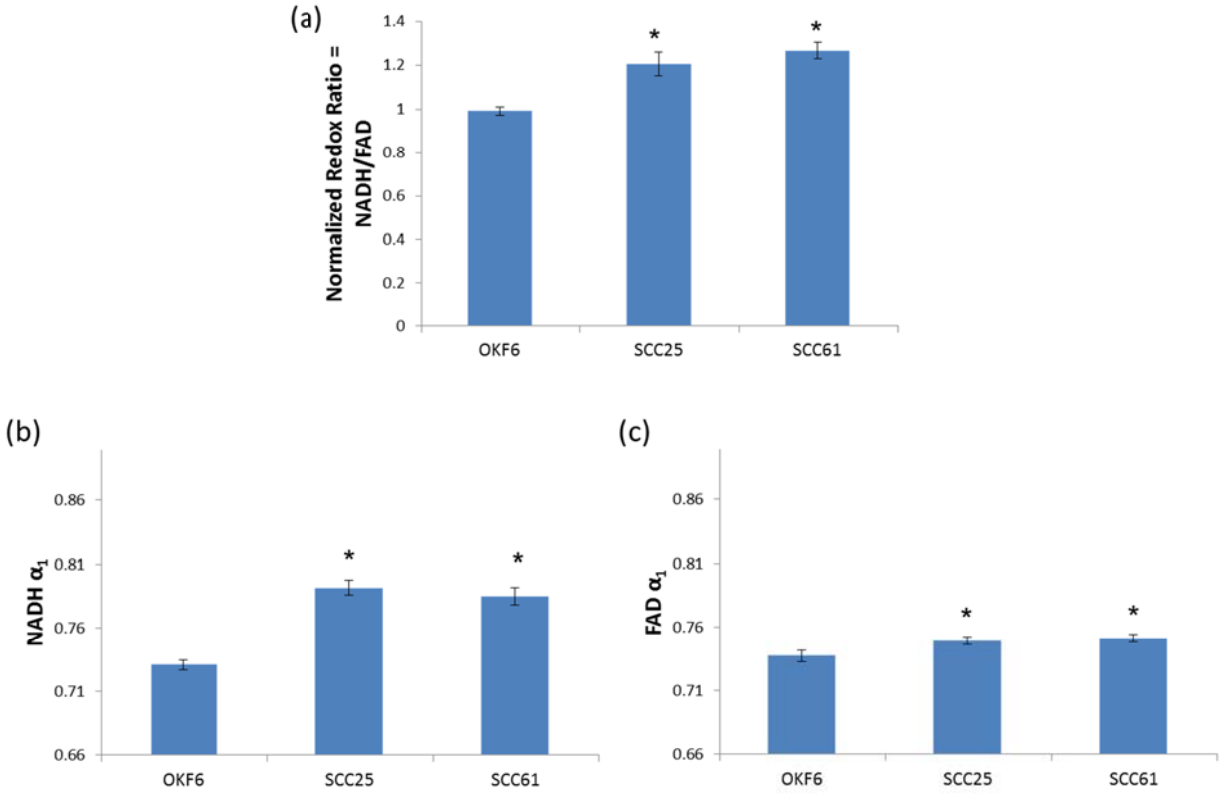

Figure 9. Optical metabolic endpoints distinguish malignant from nonmalignant cells. (a) The normalized redox ratio increases for the malignant cell lines (SCC25 and SCC61) compared to nonmalignant cells (OKF6), indicating increased glycolysis compared with oxidative phosphorylation. (b-c) The contribution of free NADH and protein-bound FAD (α_1) increase for the malignant cell lines compared with the nonmalignant cell line, reflecting shifts in metabolic pathways. * $p<0.05$, rank sum test; mean ± SEM.

The targeted treatments were validated by western blot (Figure 10). Cetuximab targeting of EGFR was assessed by measuring phosphorylated EGFR (pEGFR), which is absent with cetuximab treatment. BGT226 targeting of PI3K/mTOR was assessed by measuring phosphorylated Akt (pAkt) because PI3K and mTOR activation drive Akt activation in the

PI3K/Akt signaling pathway. pAkt is absent with BGT226 treatment. These results indicate that cetuximab and BGT226 target EGFR and PI3K/mTOR, respectively. Western blot was also performed to characterize the SCC25 and SCC61 cell lines (not shown). SCC61 cells showed increased pAkt, reflecting upregulated PI3K. Additionally, SCC61 cells exhibited increased EGFR and pEGFR compared with SCC25 cells.

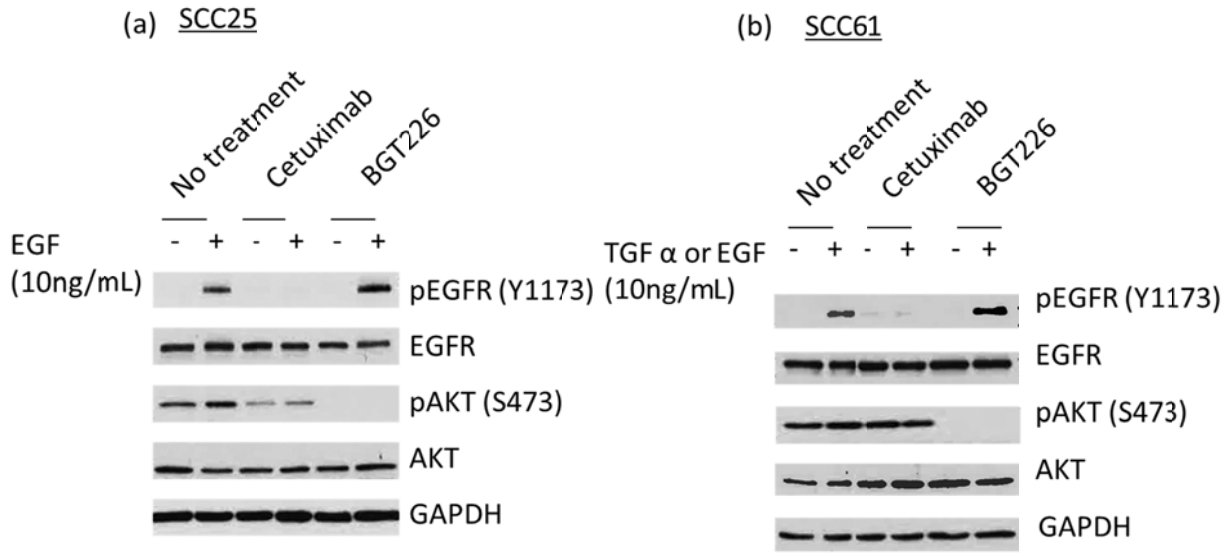

Figure 10. Western blot verifies molecular targeting of cetuximab and BGT226. Western blot for (a) SCC25 and (b) SCC61 cells. Epidermal growth factor (EGF) and transforming growth factor alpha (TGF α) activate the epidermal growth factor receptor (EGFR) and AKT pathways. Treatment with cetuximab decreases phosphorylated EGFR (pEGFR), and treatment with BGT226 decreases phosphorylated AKT (pAKT).

Representative images of SCC25 and SCC61 cells after 24 hours of treatment provide qualitative visualization of the redox ratio, NADH α_1, and FAD α_1 (Figure 11). NADH and FAD fluorescence from the cytoplasm was quantified across treatment groups and cell lines. The redox ratios of SCC25 and SCC61 cells show no significant changes with cetuximab treatment, and decrease with BGT226 and cisplatin treatment (Figure 12a). The fluorescence lifetimes of NADH and FAD reflect cellular microenvironment and protein-binding. NADH α_1 represents the

contribution from free NADH. For SCC25 cells, NADH α_1 decreases with BGT226 and cisplatin treatment. For SCC61 cells, NADH α_1 decreases with cetuximab, BGT226, and cisplatin treatment (Figure 12b). FAD α_1 represents the contribution from protein-bound FAD. For SCC25 and SCC61 cells, FAD α_1 decreases with cisplatin treatment (Figure 12c).

Proliferation was quantified as a standard measure of treatment response. Cetuximab treatment does not cause a statistically significant effect on proliferation, whereas BGT226 and cisplatin treatment decrease proliferation (Figure 12d). Additionally, glycolytic rates were quantified after treatment. SCC25 shows decreased lactate production/glucose consumption with BGT226 and cisplatin treatment, and SCC61 shows decreased lactate production/glucose consumption with cetuximab, BGT226, and cisplatin treatment (Figure 12e).

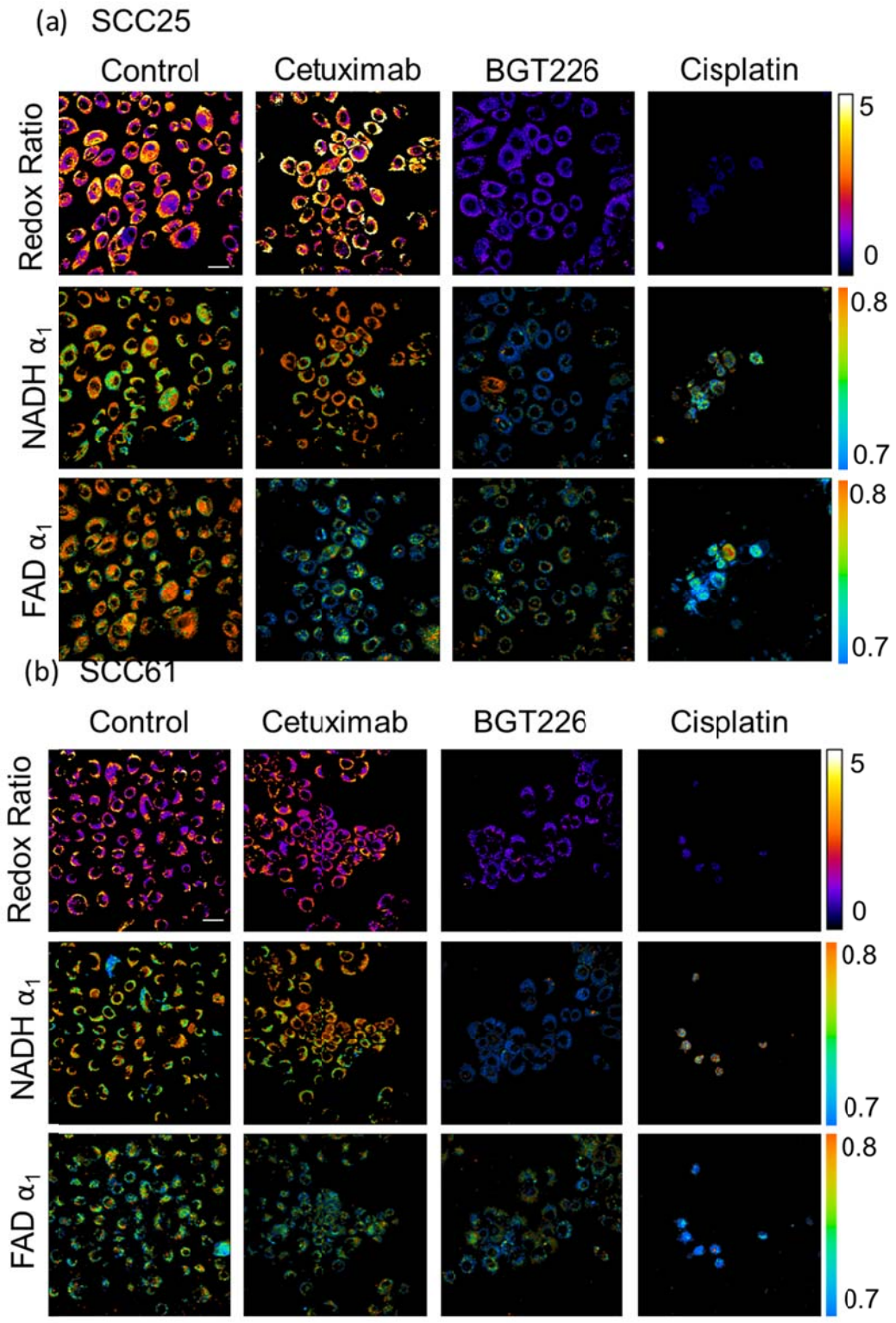

Figure 11. Representative autofluorescence images after treatment. Representative images of the redox ratio (1st row), NADH α_1 (2nd row), and FAD α_1 (third row) for (a) SCC25 cells and (b) SCC61 cells treated with control (1st column), cetuximab (2nd column), BGT226 (3rd column), or cisplatin (4th column). α_1 quantifies the short lifetime component ($\alpha_1+\alpha_2=1$). NADH α_1 represents the contribution from free NADH, while FAD α_1 conversely represents the contribution from protein-bound FAD. Scale bar represents 30um.

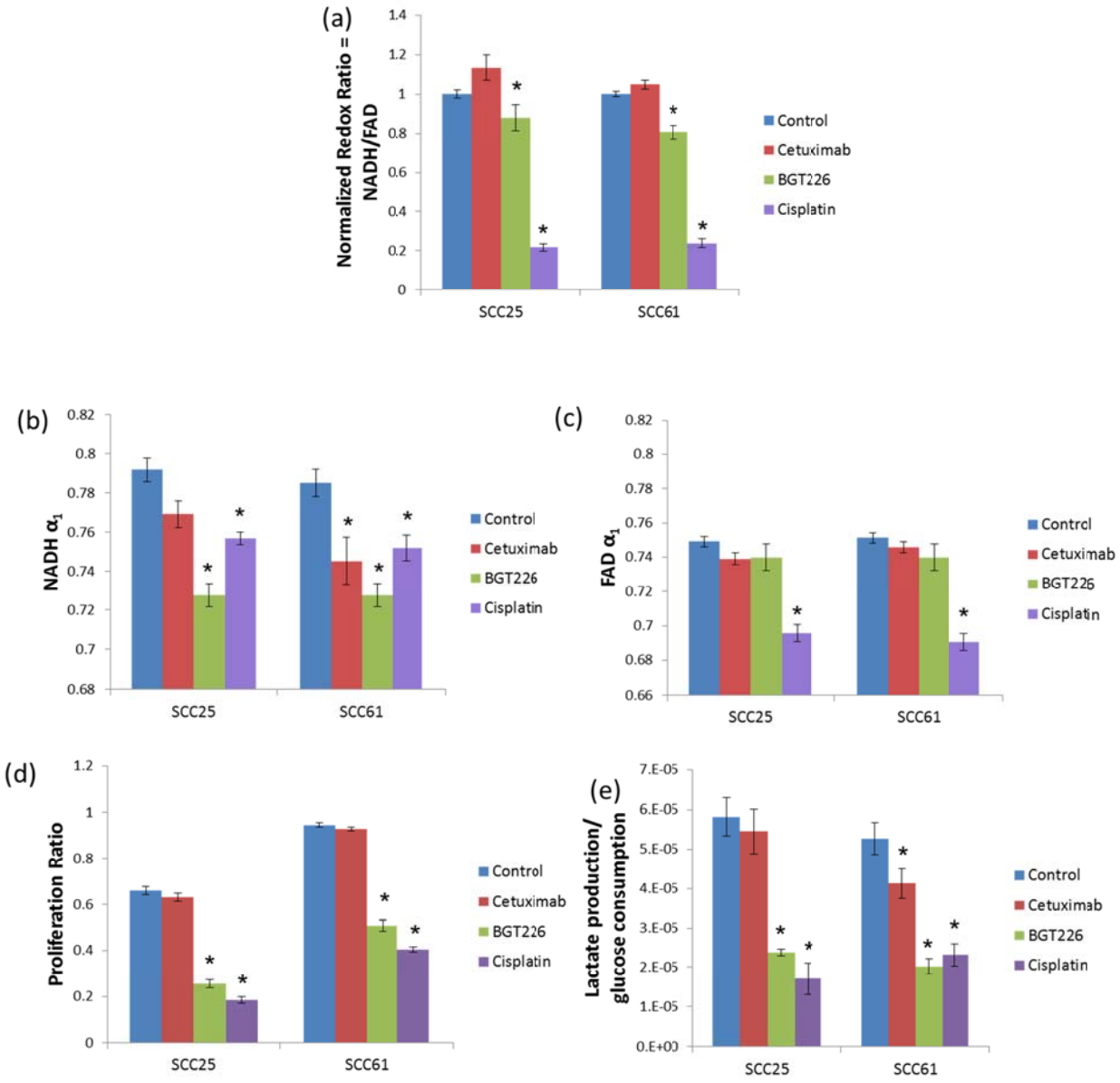

Figure 12. Metabolic endpoints measure response in SCC25 and SCC61 after treatment. (a) SCC25 and SCC61 cells were treated with cetuximab, BGT226, or cisplatin for 24 hours. The optical redox ratio is defined as the fluorescence intensity of NADH divided by that of FAD and is normalized by the redox ratio from control cells per day. Treatment with cetuximab does not affect the normalized redox ratio. Treatment with BGT226 or cisplatin decrease the normalized redox ratio. α_1 represents the contribution of the short fluorescence lifetime (free conformation for NADH and protein-bound conformation for FAD) ($\alpha_1+\alpha_2=1$). (b) NADH α_1 decreases after treatment with BGT226 and cisplatin in SCC25 cells and after treatment with cetuximab, BGT226, and cisplatin in SCC61 cells. (c) FAD α_1 decreases after treatment with cisplatin in SCC25 and SCC61 cells. (d) Cells were treated for 24 hours and proliferating cells were labeled

with BrdU. The ratio of proliferating cells was calculated by dividing the number of BrdU-labeled cells by the total number of cells per image. Treatment with cetuximab does not affect proliferation. Treatment with BGT226 or cisplatin treatment decrease proliferation. (e) The ratio of lactate production/glucose consumption reflects rates of glycolysis, which decreases after treatment with BGT226 and cisplatin in SCC25 cells and after treatment with cetuximab, BGT226, and cisplatin in SCC61 cells. * $p<0.05$ rank sum test, compared with control; mean ± SEM.

For SCC25 (Table 1a), the free and protein-bound lifetimes of NADH and FAD (τ_1 and τ_2, respectively) show no significant change with any treatment (Table 1a). The NADH mean lifetime (τ_m) shows no change for any treatment, and the FAD mean lifetime increases with cisplatin treatment ($p<0.05$). For SCC61 (Table 1b), free and protein-bound NADH lifetimes show no significant change with cetuximab and BGT226 treatment and increase with cisplatin treatment ($p<0.05$). For SCC61, the protein-bound FAD lifetime (τ_1) shows no change with any treatment, and the free FAD lifetime (τ_2) increases with cisplatin treatment ($p<0.05$). The NADH mean lifetime (τ_m) increases with BGT226 and cisplatin treatment ($p<0.05$), and the FAD mean lifetime increases with cisplatin treatment ($p<0.05$). NADH and FAD α_1 are also listed in Table 1.

Table 1. NADH and FAD fluorescence lifetimes in SCC25 and SCC61 cells after treatment with cetuximab, BGT226, or cisplatin. The short and long fluorescence lifetime components (τ_1 and τ_2, respectively), mean lifetime (τ_m), and contribution of the short lifetime component (α_1) of NADH and FAD in SCC25 (a) and SCC61 (b) after treatment. * $p<0.05$ rank sum test, compared with control; mean ± SEM.

(a)	SCC25				
		Control	Cetuximab	BGT226	Cisplatin
NADH	τ_1 (ps)	528 ± 29	526 ± 34	468 ± 27	569 ± 37
	τ_2 (ps)	2899 ± 53	2889 ± 56	2726 ± 43	2955 ± 62
	τ_m (ps)	1019 ± 37	1068 ± 39	1083 ± 36	1130 ± 46
	α_1	0.792 ± 0.006	0.769 ± 0.007	0.728 ± 0.006 *	0.757 ± 0.003 *
FAD	τ_1 (ps)	426 ± 24	396 ± 20	372 ± 19	378 ± 18
	τ_2 (ps)	2667 ± 33	2624 ± 29	2633 ± 24	2630 ± 20
	τ_m (ps)	983 ± 30	913 ± 28	959 ± 33	1059 ± 29 *
	α_1	0.749 ± 0.003	0.746 ± 0.003	0.74 ± 0.008	0.696 ± 0.005 *

(b)	SCC61				
		Control	Cetuximab	BGT226	Cisplatin
NADH	τ_1 (ps)	480 ± 26	486 ± 40	460 ± 19	796 ± 54 *
	τ_2 (ps)	2760 ± 43	2763 ± 62	2673 ± 34	3335 ± 60 *
	τ_m (ps)	968 ± 28	1064 ± 50	1083 ± 36 *	1398 ± 50 *
	α_1	0.785 ± 0.007	0.745 ± 0.012 *	0.728 ± 0.006 *	0.752 ± 0.007 *
FAD	τ_1 (ps)	432 ± 25	363 ± 12	381 ± 20	450 ± 23
	τ_2 (ps)	2654 ± 35	2546 ± 15	2667 ± 28	2713 ± 25 *
	τ_m (ps)	978 ± 31	913 ± 17	959 ± 33	1142 ± 30 *
	α_1	0.751 ± 0.003	0.746 ± 0.003	0.74 ± 0.008	0.691 ± 0.005 *

Discussion

Optimized treatment regimens have potential to improve quality of life for HNSCC patients. The goal of this study is to characterize optical metabolic imaging for early assessment of treatment efficacy. The HNSCC cell lines SCC25 and SCC61 were treated with targeted therapies (cetuximab and BGT226) and chemotherapy (cisplatin) for 24 hours, and the optical redox ratio and fluorescence lifetimes of NADH and FAD were quantified. These molecular-level measurements that reflect cellular metabolism could resolve anti-cancer treatment effects sooner than current imaging modalities, including CT, MRI, and PET. Early measurement of

treatment efficacy could accelerate drug screening and identify optimal treatment regimens for individual patients, thereby improving patient outcomes.

Isolation of NADH and FAD fluorescence emission was verified using cyanide perturbation (Figure 8). These shifts in the redox ratio and NADH and FAD lifetimes match published results [46][58][60][61]. Optical metabolic imaging distinguishes the malignant SCC25 and SCC61 cell lines from the nonmalignant OKF6 cell line (Figure 9). The increased redox ratio in HNSCC cells reflects increased reliance on glycolysis compared with oxidative phosphorylation, as expected in cancer cells (Warburg effect), and oncogene addiction, particularly to EGFR or PI3K, would be expected to increase the redox ratio [44]. This result agrees with previous findings that the redox ratio reports changes with malignancy [62]. The altered NADH and FAD fluorescence lifetimes reflect distinct signaling pathways in the HNSCC cells compared with nonmalignant cells. HNSCC cells exhibit modified intrinsic metabolic signaling that changes NADH binding sites [63], and the fluorescence lifetimes have been shown to change when NADH or FAD are bound to different enzymes [37]. Previous studies have also shown that fluorescence lifetime imaging distinguishes normal from precancer in the DMBA-treated hamster cheek pouch model [49][50].

Changes in the redox ratio across treatment groups are consistent with proliferation rates after treatment. The redox ratio is a global measure of cellular metabolism, which drives proliferation. The redox ratio and proliferation ratio are unaffected by cetuximab treatment and show statistical differences with BGT226 and cisplatin treatment (Figure 12). The lack of effect from cetuximab treatment could be attributed to *in vitro* application as a single agent. *In vivo*, cetuximab initiates antibody-dependent cell-mediated cytotoxicity (ADCC) by binding to EGFR and recruiting natural killer cells and macrophages to digest the targeted cell. However, immune

cells are not present in these cell culture studies. Additionally, cetuximab is maximally effective in combination with radiotherapy and chemotherapy because it inhibits DNA repair mechanisms [17]. Conversely, BGT226 and cisplatin actively cause cell death in cell culture. BGT226 causes cell death by autophagy [43]. Cisplatin initiates apoptosis by crosslinking DNA, which interferes with mitosis and causes failure of DNA repair [64]. No previous literature has reported the effects of cetuximab or BGT226 on the optical redox ratio. Cisplatin has been shown to increase NADH and FAD fluorescence intensity and decrease FAD/(NADH+FAD) after 9 hours of treatment with 33μM cisplatin in primary human foreskin keratinocytes [65]. These results indicate a greater increase in NADH than FAD, which contradicts our measured decrease in NADH/FAD 24h after 176μM cisplatin treatment in SCC25 and SCC61 cells (Figure 12). However, the time-course of response, cell type-specific processes for cell death, and different concentrations of cisplatin could explain the differences in redox ratio.

The contribution from free NADH (NADH α_1) shows shifts in protein-binding of NADH with BGT226 and cisplatin treatment in SCC25 and SCC61 cells as well as with cetuximab treatment in SCC61 cells (Figure 12b). The ratio of lactate production divided by glucose consumption reflects amounts of terminal glycolysis compared with total glucose metabolism. In glycolysis, glucose is consumed and pyruvate is produced. Pyruvate is either fermented into lactate as a terminal stage of glycolysis or converted to acetyl-coA as fuel for the citric acid cycle. Cetuximab treatment does not affect glycolysis rates in SCC25, but decreases glycolysis in SCC61. The decrease in glycolysis and NADH α_1 in SCC61 cells indicates shifts in metabolic pathways in response to treatment. However, proliferation is not affected by cetuximab in SCC61, indicating compensation by effectors downstream of EGFR. Cetuximab has been shown to not affect short-term cell growth in SCC25, which could explain the lack of statistical

significance in the NADH α_1 and glycolytic index [66]. BGT226 and cisplatin treatments decrease glycolysis in SCC25 and SCC61. The effect of cetuximab or BGT226 on SCC61 cells has not been cited in previous literature, and the effect of BGT226 on glycolysis has not been reported in any model. The measurement of glycolysis rates calculated by lactate production/glucose consumption is correlated with NADH α_1 (0.81 Pearson's correlation coefficient, $p<0.05$). No other measurements produced a statistically significant correlation coefficient with lactate production/glucose consumption or proliferation. Cisplatin treatment produces outliers that impacted the correlations, particularly between lactate production/glucose consumption and the redox ratio. Previous studies have shown a correlation between glucose uptake/lactate production and the optical redox ratio in breast cancer cells [46]. However, this correlation was determined for basal metabolic rates in cells without treatment, and cells from a different organ site could rely on different metabolic mechanisms. Additionally, the control SCC61 cells show a higher proliferation ratio than SCC25 ($p<0.05$) (Figure 12d), but no statistical difference in redox ratio (Figure 9a). This is in contrast to the similar lactate production/glucose consumption between the control SCC25 and SCC61. Although the trends in NADH α_1 and redox ratio agree with the gold standards, they are not surrogate measurements of proliferation or the amount of glycolysis compared with total glucose metabolism. For example, alternative metabolic pathways such as beta oxidation of fatty acids, the pentose phosphate pathway, and glutaminolysis are all captured differently by these gold standard measurements and our optical measurements [67][68]. The contribution from protein-bound FAD (FAD α_1) is unaffected by cetuximab and BGT226 treatments and decreases with cisplatin treatment (Figure 12c).

Early measures of treatment response could enable effective intervention while reducing the acute toxicities and serious morbidities from ineffective therapies. Molecular-level measurements that reflect cellular metabolism are well-suited to measure effects from cancer treatments that target metabolic pathways. The optical redox ratio and fluorescence lifetimes of NADH and FAD resolve a response after 24 hours of treatment with targeted therapies and chemotherapies in HNSCC cells. These results indicate that optical metabolic imaging shows promise to identify effective drug candidates during drug development. Additionally, applying optical metabolic imaging to measure treatment response early has potential to impact quality of life for HNSCC patients.

CHAPTER 3

CONCLUSION AND FUTURE DIRECTIONS

The current standard to measure cancer treatment response includes whole-body imaging, like PET, CT, x-ray, and MRI. However, these methods could be complemented with a molecular-level tool that utilizes endogenous contrast to measure treatment efficacy soon after therapy in HNSCC patients. This study exploits the autofluorescence intensities and lifetimes from the metabolic cofactors NADH and FAD to quantify treatment response in two HNSCC cell lines. Response was measured after 24 hours of treatment. Gold standard protocols for assessing treatment response, including western blot analysis, proliferation rate quantification, and glycolytic rate quantification, also measured response after treatment. These results indicate that optical metabolic endpoints have potential to measure early response to therapy in HNSCC.

Future work will include the characterization of optical metabolic imaging in a more complex *in vitro* model, the application of optical metabolic imaging *in vivo*, and the design of a clinical system to measure these optical endpoints in HNSCC patients. Xenografts of human HNSCC cell lines will be grown in nude mice. In an initial study, tumors will be excised, digested, and grown in culture as organoids. These organoids will contain the cancer cells as well as the immune cells, fibroblasts, and other cell types growing in the tumor. This interaction of cell types will better mimic the complex *in vivo* tumor environment. The organoids will be treated with anti-cancer drugs and optical metabolic endpoints will be characterized. Gold standard response will include tumor growth curves in a separate cohort of mice.

In a separate study, mice with HNSCC xenografts will be administered anti-cancer treatments, and two-photon fluorescence microscopy and fluorescence lifetime imaging will be

conducted *in vivo*. This study will harness the deep penetration and intrinsic depth sectioning of two-photon fluorescence excitation to quantify optical metabolic endpoints on a cellular-level resolution. This study will establish feasibility of these measurements *in vivo*. Gold standard measurements of proliferation and cell death will be quantified using histology as well as tumor growth curves in a separate cohort of mice.

In vivo microscopy results will serve as measurements from an ideal system with high spatial, axial, and temporal resolution. Analysis will be conducted to determine the minimum requirements for a clinical system to be used in HNSCC patients. Data will be analyzed on a per-cell basis compared with a per-image basis to determine minimum resolution requirements. Additionally, analysis using automated criteria for thresholding as well as no thresholding will be compared to determine thresholding requirements. Fluorescence lifetime decay curves will be undersampled to determine the minimum time resolution necessary for lifetime quantification.

Optical metabolic imaging has potential to measure treatment response in HNSCC patients soon after therapy. Additionally, optical metabolic imaging could be implemented in preclinical models to screen for effective drugs and accelerate drug development. Furthermore, optical metabolic imaging could serve as a platform to predict optimal treatment regimens before administering therapy to patients. Improved treatment regiments and early assessment of treatment response in HNSCC patients has potential to reduce the morbidities and toxicities associated with ineffective therapy and to improve patient outcomes.

REFERENCES

[1] L. Sherwood, *Human Physiology: From Cells to Systems*, Sixth. Belmont, CA: Thompson Brooks/Cole, 2007.

[2] N. C. Institute, "Epithelial Tissue." [Online]. Available: http://training.seer.cancer.gov/anatomy/cells_tissues_membranes/tissues/epithelial.html.

[3] J. Campbell, Neil Reece, "Basic Principles of Animal Form and Function," in in *Biology*, Seventh., B. Wilbur, Beth Gale, Deborah Burner, Pat Winichoff, Ed. San Fancisco, CA: Pearson Education, Inc., 2005, pp. 823–824.

[4] C. Royer and X. Lu, "Epithelial cell polarity: a major gatekeeper against cancer?," *Cell Death Differ.*, vol. 18, no. 9, pp. 1470–7, Sep. 2011.

[5] V. Backman, M. B. Wallace, L. T. Perelman, J. T. Arendt, R. Gurjar, M. G. Müller, Q. Zhang, G. Zonios, E. Kline, J. a McGilligan, S. Shapshay, T. Valdez, K. Badizadegan, J. M. Crawford, M. Fitzmaurice, S. Kabani, H. S. Levin, M. Seiler, R. R. Dasari, I. Itzkan, J. Van Dam, M. S. Feld, and T. McGillican, "Detection of preinvasive cancer cells.," *Nature*, vol. 406, no. 6791, pp. 35–6, Jul. 2000.

[6] R. Weinberg, *The Biology of Cancer*. Taylor & Francis, 2006.

[7] N. C. I. at the N. I. of Health, "Oropharyngeal Cancer Treatment," 2012. [Online]. Available: http://www.cancer.gov/cancertopics/pdq/treatment/oropharyngeal/Patient/page1. [Accessed: 18-Sep-2012].

[8] J. P. Shah and W. Lydiatt, "Treatment of cancer of the head and neck.," *CA. Cancer J. Clin.*, vol. 45, no. 6, pp. 352–68.

[9] M. J. Hayat, N. Howlader, M. E. Reichman, and B. K. Edwards, "Cancer statistics, trends, and multiple primary cancer analyses from the Surveillance, Epidemiology, and End Results (SEER) Program.," *Oncologist*, vol. 12, no. 1, pp. 20–37, Jan. 2007.

[10] J. Massano, F. S. Regateiro, G. Januário, and A. Ferreira, "Oral squamous cell carcinoma: review of prognostic and predictive factors.," *Oral Surg. Oral Med. Oral Pathol. Oral Radiol. Endod.*, vol. 102, no. 1, pp. 67–76, Jul. 2006.

[11] M. Gillison, "Human papillomavirus-associated head and neck cancer is a distinct epidemiologic, clinical, and molecular entity," *Semin Oncol*, vol. 31, no. 6, pp. 744–754, 2004.

[12] W. PC, A. KE, B. AT, and M. TR, “Carcinoma of the hypopahrynx: analysis of incidence and survival in Sweden over a 30-year period.,” *Head Neck*, vol. 20, no. 8, pp. 714–719, 1998.

[13] N. C. I. at the N. I. of Health, “Head and Neck Cancers,” 2012. [Online]. Available: http://www.cancer.gov/cancertopics/factsheet/Sites-Types/head-and-neck. [Accessed: 24-Sep-2012].

[14] J. Suen and S. Stern, “Cancer of the head and neck,” *Cancer Head Neck*, vol. 462–484, 1996.

[15] S. Marur and A. a Forastiere, “Head and neck cancer: changing epidemiology, diagnosis, and treatment.,” *Mayo Clin. Proc.*, vol. 83, no. 4, pp. 489–501, Apr. 2008.

[16] D. S. Salomon, R. Brandta, F. Ciardiellob, and N. Normannoc, “Epidermal growth factor-related peptides and their receptors in human malignancies,” *Crit. Rev. Oncol. Hematol.*, vol. 19, no. 94, 1995.

[17] J. Bernier, S. M. Bentzen, and J. B. Vermorken, “Molecular therapy in head and neck oncology.,” *Nat. Rev. Clin. Oncol.*, vol. 6, no. 5, pp. 266–77, May 2009.

[18] P. Harari, D. Wheeler, and J. Grandis, “Molecular Target Approaches in Head and Neck Cancer: EGFR and Beyond,” *Semin Radiat Oncol*, vol. 19, no. 1, pp. 63–68, 2009.

[19] J. Egloff, Ann Grandis, “Targeting EGFR and Src Pathways in Head and Neck Cancer,” *Semin. Oncol.*, vol. 35, no. 3, pp. 286–297, 2008.

[20] C. Leemans, R. Tiwari, J. Nauta, I. van der Wall, and G. Snow, “Recurrence at the primary site in head and neck cancer and the significance of neck lymph node metastases as a prognostic factor,” *Cancer*, vol. 73, no. 1, pp. 187–190, 1994.

[21] a Rousseau and C. Badoual, “Head and Neck: Squamous cell carcinoma: an overview,” *Atlas of Genetics and Cytogenetics in Oncology and Haematology*, no. 2. Mar-2012.

[22] a Psyrri, M. Kwong, S. DiStasio, L. Lekakis, M. Kassar, C. Sasaki, L. D. Wilson, B. G. Haffty, Y. H. Son, D. a Ross, P. M. Weinberger, G. G. Chung, D. Zelterman, B. a Burtness, and D. L. Cooper, “Cisplatin, fluorouracil, and leucovorin induction chemotherapy followed by concurrent cisplatin chemoradiotherapy for organ preservation and cure in patients with advanced head and neck cancer: long-term follow-up.,” *J. Clin. Oncol.*, vol. 22, no. 15, pp. 3061–9, Aug. 2004.

[23] P. M. Vila, C. W. Park, M. C. Pierce, G. H. Goldstein, L. Levy, V. V Gurudutt, A. D. Polydorides, J. H. Godbold, M. S. Teng, E. M. Genden, B. a Miles, S. Anandasabapathy, A. M. Gillenwater, R. Richards-Kortum, and A. G. Sikora, “Discrimination of Benign and Neoplastic Mucosa with a High-Resolution Microendoscope (HRME) in Head and Neck Cancer.,” *Ann. Surg. Oncol.*, Apr. 2012.

[24] K. C. Maitland, A. M. Gillenwater, M. D. Williams, A. K. El-Naggar, M. R. Descour, and R. R. Richards-Kortum, "In vivo imaging of oral neoplasia using a miniaturized fiber optic confocal reflectance microscope.," *Oral Oncol.*, vol. 44, no. 11, pp. 1059–66, Nov. 2008.

[25] D. Heintzelman, U. Utzinger, and H. Fuchs, "Optimal excitation wavelengths for in vivo detection of oral neoplasia using fluorescence spectroscopy," *Photochem Photobiol*, vol. 72, pp. 103–113, 2000.

[26] K. Sokolov, R. Drezek, K. Gossage, and R. Richards-Kortum, "Reflectance spectroscopy with polarized light: is it sensitive to cellular and nuclear morphology.," *Opt. Express*, vol. 5, no. 13, pp. 302–17, Dec. 1999.

[27] M. G. Müller, T. a Valdez, I. Georgakoudi, V. Backman, C. Fuentes, S. Kabani, N. Laver, Z. Wang, C. W. Boone, R. R. Dasari, S. M. Shapshay, and M. S. Feld, "Spectroscopic detection and evaluation of morphologic and biochemical changes in early human oral carcinoma.," *Cancer*, vol. 97, no. 7, pp. 1681–92, Apr. 2003.

[28] M. Huber, S. Bsoul, and G. Terezhalmy, "Acetic acid wash and chemiluminescent illumination as an adjunct to conventional oral soft tissue examination for the detection of dysplasia: pilot study," *Quntessence Int*, vol. 35, pp. 378–384, 2004.

[29] E. E. Helman, J. R. Newman, N. R. Dean, W. Zhang, K. R. Zinn, and E. L. Rosenthal, "Optical imaging predicts tumor response to anti-EGFR therapy," *Cancer Biol. Ther.*, vol. 10, no. 2, pp. 166–171, Jul. 2010.

[30] J. P. Gleysteen, R. D. Duncan, J. S. Magnuson, J. B. Skipper, K. Zinn, and E. L. Rosenthal, "Fluorescently labeled cetuximab to evaluate head and neck cancer response to treatment.," *Cancer Biol. Ther.*, vol. 6, no. 8, pp. 1181–5, Aug. 2007.

[31] J. Lakowicz, *Principles of fluorescence spectroscopy*. New York: Plenum Publishers, 1999.

[32] N. Ramanujam, "Fluorescence spectroscopy of neoplastic and non-neoplastic tissues.," *Neoplasia*, vol. 2, no. 1–2, pp. 89–117, 2000.

[33] W. Denk, J. Strickler, and W. Webb, "Two-photon laser scanning fluorescence microscopy," *Science (80-.).*, vol. 248, pp. 73–76, 1990.

[34] F. Helmchen and W. Denk, "Deep tissue two-photon microscopy," vol. 2, no. 12, 2005.

[35] Z. Benediktyová and L. Nedbal, "Imaging of multi-color fluorescence emission from leaf tissues.," *Photosynth. Res.*, vol. 102, no. 2–3, pp. 169–75, 2009.

[36] LOCI and U. of Wisconsin-Madison, "Multiple-photon Excitation Fluorescence Microscopy," 2013. [Online]. Available: http://loci.wisc.edu/optical-sectioning/multiple-photon-excitation-fluorescence-microscopy.

[37] J. R. Lakowicz, H. Szmacinski, K. Nowaczyk, and M. L. Johnson, "Fluorescence lifetime imaging of free and protein-bound NADH.," *Proc. Natl. Acad. Sci. U. S. A.*, vol. 89, no. 4, pp. 1271–5, Feb. 1992.

[38] F. I. B Chance, B Schoener, R Oshino, "Oxidation-reduction ratio studies of mitochondria in freeze-trapped samples. NADH and flavoprotein fluorescence signals.," *J. Biol. Chem.*, vol. 254, pp. 4764–4771, 1979.

[39] C. Fung and J. Grandis, "Emerging drugs to treat squamous cell carcinomas of the head and neck," *Expert Opin Emerg Drugs*, vol. 15, no. 3, pp. 355–373, 2010.

[40] S. K. Kundu and M. Nestor, "Targeted therapy in head and neck cancer.," *Tumour Biol.*, vol. 33, no. 3, pp. 707–21, Jun. 2012.

[41] L. B. Saltz, N. J. Meropol, P. J. Loehrer, M. N. Needle, J. Kopit, and R. J. Mayer, "Phase II trial of cetuximab in patients with refractory colorectal cancer that expresses the epidermal growth factor receptor.," *J. Clin. Oncol.*, vol. 22, no. 7, pp. 1201–8, Apr. 2004.

[42] J. M. G. Pedrero, D. G. Carracedo, C. M. Pinto, A. H. Zapatero, J. P. Rodrigo, C. S. Nieto, and M. V. Gonzalez, "Frequent genetic and biochemical alterations of the PI 3-K/AKT/PTEN pathway in head and neck squamous cell carcinoma.," *Int. J. Cancer*, vol. 114, no. 2, pp. 242–8, Mar. 2005.

[43] K.-Y. Chang, S.-Y. Tsai, C.-M. Wu, C.-J. Yen, B.-F. Chuang, and J.-Y. Chang, "Novel phosphoinositide 3-kinase/mTOR dual inhibitor, NVP-BGT226, displays potent growth-inhibitory activity against human head and neck cancer cells in vitro and in vivo.," *Clin. Cancer Res.*, vol. 17, no. 22, pp. 7116–26, Nov. 2011.

[44] O. Warburg, "On the origin of cancer cells," *Science (80-.).*, vol. 123, pp. 309–314, 1956.

[45] J. H. Ostrander, C. M. McMahon, S. Lem, S. R. Millon, J. Q. Brown, V. L. Seewaldt, and N. Ramanujam, "Optical redox ratio differentiates breast cancer cell lines based on estrogen receptor status.," *Cancer Res.*, vol. 70, no. 11, pp. 4759–66, Jun. 2010.

[46] A. J. Walsh, R. S. Cook, H. C. Manning, D. J. Hicks, A. Lafontant, C. L. Arteaga, and M. C. Skala, "Optical Metabolic Imaging Identifies Glycolytic Levels, Subtypes, and Early-Treatment Response in Breast Cancer.," *Cancer Res.*, vol. 73, no. 20, pp. 6164–6174, Oct. 2013.

[47] I. Pavlova, M. Williams, A. El-Naggar, R. Richards-Kortum, and A. Gillenwater, "Understanding the biological basis of autofluorescence imaging for oral cancer detection:

high-resolution fluorescence microscopy in viable tissue.," *Clin. Cancer Res.*, vol. 14, no. 8, pp. 2396–404, Apr. 2008.

[48] M. C. Skala, K. M. Riching, D. K. Bird, A. Gendron-fitzpatrick, J. Eickhoff, K. W. Eliceiri, P. J. Keely, and N. Ramanujam, "In vivo Multiphoton Fluorescence Lfetime Imaging of Protein-bound and Free NADH in Normal and Pre-cancerous Epithelia," *JBO*, vol. 12, no. 2, pp. 1–19, 2007.

[49] M. C. Skala, K. M. Riching, A. Gendron-Fitzpatrick, J. Eickhoff, K. W. Eliceiri, J. G. White, and N. Ramanujam, "In vivo multiphoton microscopy of NADH and FAD redox states, fluorescence lifetimes, and cellular morphology in precancerous epithelia.," *Proc. Natl. Acad. Sci. U. S. A.*, vol. 104, no. 49, pp. 19494–9, Dec. 2007.

[50] J. M. Jabbour, S. Cheng, B. H. Malik, R. Cuenca, J. a Jo, J. Wright, Y.-S. L. Cheng, and K. C. Maitland, "Fluorescence lifetime imaging and reflectance confocal microscopy for multiscale imaging of oral precancer.," *J. Biomed. Opt.*, vol. 18, no. 4, p. 046012, Apr. 2013.

[51] Y. Sun, J. Phipps, D. S. Elson, H. Stoy, S. Tinling, J. Meier, B. Poirier, F. S. Chuang, D. G. Farwell, and L. Marcu, "Fluorescence lifetime imaging microscopy: in vivo application to diagnosis of oral carcinoma.," *Opt. Lett.*, vol. 34, no. 13, pp. 2081–3, Jul. 2009.

[52] M. C. Skala, J. M. Squirrell, K. M. Vrotsos, C. Squamous, J. C. Eickhoff, A. Gendron-fitzpatrick, K. W. Eliceiri, and N. Ramanujam, "Multiphoton Microscopy of Endogenous Fluorescence Differentiates Normal , Precancerous , and Cancerous Squamous Epithelial Tissues Multiphoton Microscopy of Endogenous Fluorescence Differentiates Epithelial Tissues," pp. 1180–1186, 2005.

[53] J. Sun, T. Shilagard, B. Bell, M. Motamedi, and G. Vargas, "In vivo multimodal nonlinear optical imaging of mucosal tissue," *Opt. Express*, vol. 12, no. 11, pp. 2478–2486, 2004.

[54] M. a Dickson, W. C. Hahn, Y. Ino, V. Ronfard, J. Y. Wu, R. a Weinberg, D. N. Louis, F. P. Li, and J. G. Rheinwald, "Human keratinocytes that express hTERT and also bypass a p16(INK4a)-enforced mechanism that limits life span become immortal yet retain normal growth and differentiation characteristics.," *Mol. Cell. Biol.*, vol. 20, no. 4, pp. 1436–47, Feb. 2000.

[55] N. Zhang, K. Erjala, J. Kulmala, X. Qiu, M. Sundvall, K. Elenius, and R. Grénman, "Concurrent cetuximab, cisplatin, and radiation for squamous cell carcinoma of the head and neck in vitro.," *Radiother. Oncol.*, vol. 92, no. 3, pp. 388–92, Sep. 2009.

[56] R. B. Erlich, Z. Kherrouche, D. Rickwood, L. Endo-Munoz, S. Cameron, a Dahler, M. Hazar-Rethinam, L. M. de Long, K. Wooley, a Guminski, and N. a Saunders, "Preclinical evaluation of dual PI3K-mTOR inhibitors and histone deacetylase inhibitors in head and neck squamous cell carcinoma.," *Br. J. Cancer*, vol. 106, no. 1, pp. 107–15, Jan. 2012.

[57] T. Y. Seiwert, R. Jagadeeswaran, L. Faoro, V. Janamanchi, V. Nallasura, M. El Dinali, S. Yala, R. Kanteti, E. E. W. Cohen, M. W. Lingen, L. Martin, S. Krishnaswamy, A. Klein-Szanto, J. G. Christensen, E. E. Vokes, and R. Salgia, "The MET receptor tyrosine kinase is a potential novel therapeutic target for head and neck squamous cell carcinoma.," *Cancer Res.*, vol. 69, no. 7, pp. 3021–31, Apr. 2009.

[58] D. K. Bird, L. Yan, K. M. Vrotsos, K. W. Eliceiri, E. M. Vaughan, P. J. Keely, J. G. White, and N. Ramanujam, "Metabolic mapping of MCF10A human breast cells via multiphoton fluorescence lifetime imaging of the coenzyme NADH.," *Cancer Res.*, vol. 65, no. 19, pp. 8766–73, Oct. 2005.

[59] J. Eng, R. M. Lynch, and R. S. Balaban, "Nicotinamide adenine dinucleotide fluorescence spectroscopy and imaging of isolated cardiac myocytes Spectroscopy," vol. 55, no. April, 1989.

[60] S. Huang, A. a Heikal, and W. W. Webb, "Two-photon fluorescence spectroscopy and microscopy of NAD(P)H and flavoprotein.," *Biophys. J.*, vol. 82, no. 5, pp. 2811–25, May 2002.

[61] A. Walsh, R. S. Cook, B. Rexer, C. L. Arteaga, and M. C. Skala, "Optical imaging of metabolism in HER2 overexpressing breast cancer cells.," *Biomed. Opt. Express*, vol. 3, no. 1, pp. 75–85, Jan. 2012.

[62] R. Drezek, C. Brookner, I. Pavlova, I. Boiko, A. Malpica, R. Lotan, and R. Richards-kortum, "Auto fl uorescence Microscopy of Fresh Cervical-Tissue Sections Reveals Alterations in Tissue Biochemistry with Dysplasia ¶," vol. 73, no. 6, pp. 636–641, 2001.

[63] S. Banerjee and D. K. Bhatt, "Histochemical studies on the distribution of certain dehydrogenases in squamous cell carcinoma of cheek," *Indian J. Cancer*, vol. 26, pp. 21–30, 1989.

[64] A. Eastman, "The mechanism of action of cisplatin: from adducts to apoptosis," in in *Cisplatin. Chemistry and biochemistry of a leading anticancer drug*, 1999, pp. 111–134.

[65] J. M. Levitt, A. Baldwin, A. Papadakis, S. Puri, J. Xylas, K. Münger, and I. Georgakoudi, "Intrinsic fluorescence and redox changes associated with apoptosis of primary human epithelial cells.," *J. Biomed. Opt.*, vol. 11, no. 6, p. 064012, 2011.

[66] M. Nestor, "Effect of cetuximab treatment in squamous cell carcinomas.," *Tumour Biol.*, vol. 31, no. 2, pp. 141–7, Apr. 2010.

[67] I. Georgakoudi and K. P. Quinn, "Optical imaging using endogenous contrast to assess metabolic state.," *Annu. Rev. Biomed. Eng.*, vol. 14, pp. 351–67, Jan. 2012.

[68] M. Board, S. Humm, and E. a Newsholme, "Maximum activities of key enzymes of glycolysis, glutaminolysis, pentose phosphate pathway and tricarboxylic acid cycle in

normal, neoplastic and suppressed cells.," *Biochem. J.*, vol. 265, no. 2, pp. 503–9, Jan. 1990.